引用格式：李振瀚，李华，鲍晓华，等. 120 kA 脉冲电抗器在振荡放电电路中的电磁场分布优化 [J]. 南方能源建设，2024，11(3)：23-35. LI Zhenhan, LI Hua, BAO Xiaohua, et al. Optimization of electromagnetic field distribution of 120 kA pulse inductor in oscillation discharge circuit [J]. Southern energy construction, 2024, 11(3): 23-35. DOI：10.16516/j.ceec.2024.3.03.

120 kA 脉冲电抗器在振荡放电电路中的电磁场分布优化

李振瀚[1]，李华[2,✉]，鲍晓华[1]，高格[2]
（1. 合肥工业大学 电气与自动化工程学院，安徽 合肥 230009；
2. 中国科学院合肥物质科学研究院 等离子体物理研究所，安徽 合肥 230031）

摘要：[**目的**]脉冲电抗器是失超保护系统振荡放电回路中的重要组成部分。在振荡放电回路中，利用脉冲电抗器与充电电容器振荡产生高脉冲电流，使流过真空断路器的电流反向以创建人工过零点，完成开关分断。但是在通入 120 kA 电流的工况下，由于受到电磁力的作用，脉冲电抗器下方连接排会发生形变，造成设备损坏，大大降低辅助振荡过零回路的可靠性。因此需要对 120 kA 脉冲电抗器进行电磁场分析，优化其周围电磁场分布。[**方法**]首先分析辅助振荡过零电路的换流过程，建立脉冲电抗器三维模型，引入磁场屏蔽百分比的概念。其次，通过使用有限元仿真软件计算了不同材料和形状的屏蔽板对脉冲电抗器电磁场分布的影响。分析了不同材料和形状对屏蔽百分比的影响，计算了不同形状下的涡流损耗。最后在结构模块中计算了不同屏蔽结构下的连接排形变程度。[**结果**]屏蔽板采用不同材料或结构对连接排受到的磁感应强度和电磁力有影响。[**结论**]圆形铝屏蔽板对脉冲电抗器电磁场分布的优化效果更好。该方法也为脉冲电抗器的电磁屏蔽设计奠定了基础。

关键词：脉冲电抗器；屏蔽板；屏蔽百分比；辅助振荡；失超保护系统
中图分类号：TL4；TL62　　**文献标志码：**A　　**文章编号：**2095-8676(2024)03-0023-13
DOI：10.16516/j.ceec.2024.3.03　　**OA：**https://www.energychina.press/

论文二维码

Optimization of Electromagnetic Field Distribution of 120 kA Pulse Inductor in Oscillation Discharge Circuit

LI Zhenhan[1], LI Hua[2,✉], BAO Xiaohua[1], GAO Ge[2]
（1. School of Electrical Engineering and Automation, Hefei University of Technology, Hefei 230009, Anhui, China；
2. Institute of Plasma Physics, Hefei Institutes of Physical Science, Chinese Academy of Sciences, Hefei 230031, Anhui, China）

Abstract: [**Introduction**] Pulse inductor is an important component of the oscillation discharge circuit in the quench protection system. In the oscillating discharge circuit, the pulse inductor and charging capacitor are used to oscillate and generate high pulse currents, causing the current flowing through the vacuum circuit breaker to reverse and create an artificial zero-crossing point, thus completing the switch breaking. However, under the condition of 120 kA current, due to the action of the electromagnetic force, the connecting bar below the pulse inductor will deform, causing equipment damage and greatly reducing the reliability of the auxiliary oscillation zero-crossing circuit. Therefore, it is necessary to conduct electromagnetic field analysis on the 120 kA pulse inductor and optimize the electromagnetic field distribution around it. [**Method**] Firstly, the commutation process of the auxiliary oscillation zero-crossing circuit was analyzed to establish a three-dimensional model of the pulse inductor, and the concept of magnetic field shielding percentage was introduced. Secondly, the influence of shielding plates with different materials and shapes on electromagnetic field distributions was

收稿日期：2024-01-22　　**修回日期：**2024-03-16
基金项目：国家重大科技基础设施建设项目“聚变堆主机关键系统综合研究设施”（2018-000052-73-01-001228）

calculated by using finite element simulation. Then the influence of different materials and shapes on shielding percentage was analyzed, and eddy current losses under different shapes were calculated. Finally, the deformation degree of the connecting bar under different shielding structures was calculated in the structural module. [**Result**] The results show that the use of different materials or structures in the shielding plates influences the magnetic induction intensity and electromagnetic force received by the connecting bar. [**Conclusion**] The circular aluminum shielding plate has a better optimization effect for the electromagnetic field distribution. This method also lays a foundation for the electromagnetic shield design of pulse inductors.

Key words: pulse inductor; shielding plate; shielding percentage; auxiliary oscillation; quench protection system

2095-8676

0 Introduction

Large superconducting magnet[1-3] is commonly used in magnetic confinement fusion devices to provide strong magnetic field for confining the plasma. The quench accident, which means the superconductor suddenly changes from zero resistance state to normal state resistance state, can cause a rapid temperature rise with high Joule heat and even burn the magnet[4-8]. Therefore, the quench protection system (QPS)[9-12] is essential for the safe operation of superconductors.

The topology of QPS in the comprehensive research facility for fusion technology (CRAFT) is shown in Fig. 1, where the auxiliary oscillation zero-crossing circuit consists of the charging capacitor, pulse inductor and four thyristor stacks. The bypass switch carries a steady state of 100 kA current, the vacuum circuit breaker (VCB) can interrupt the high current with the auxiliary oscillation zero-crossing circuit, and the fast discharge resistor is used to consume energy stored

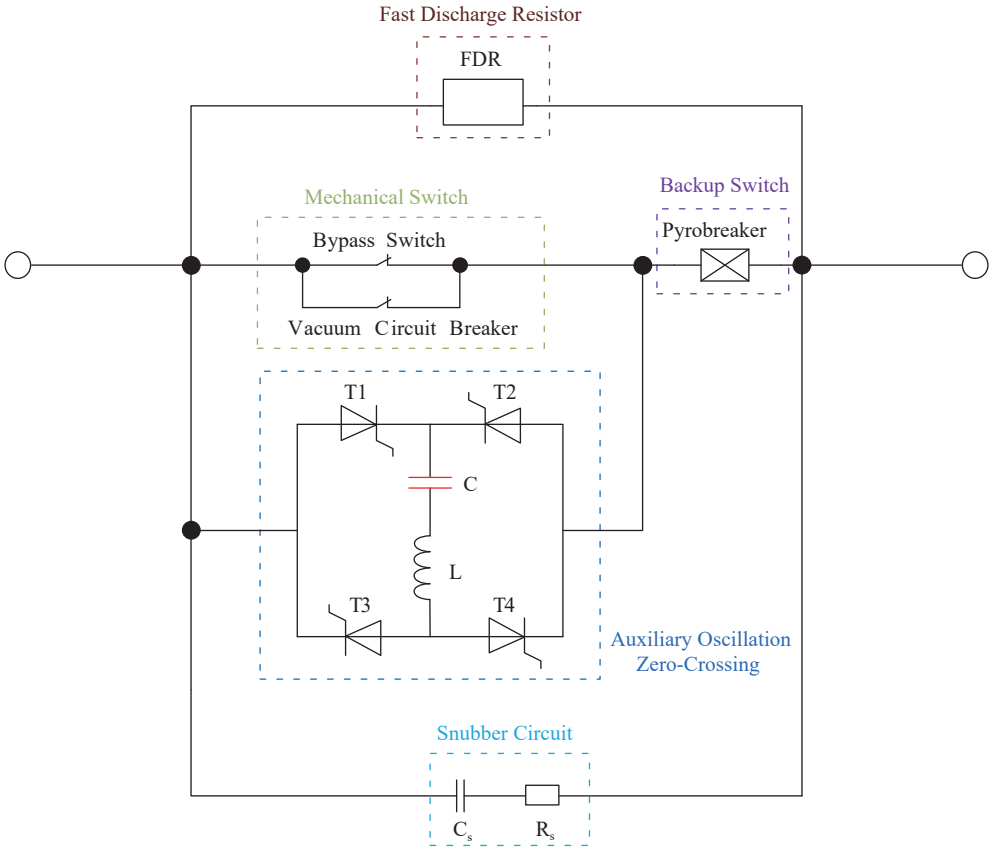

Fig. 1 Topology of QPS in CRAFT

in the magnet. The control logic and current transfer diagram of QPS[13-15] are shown in Fig. 2.

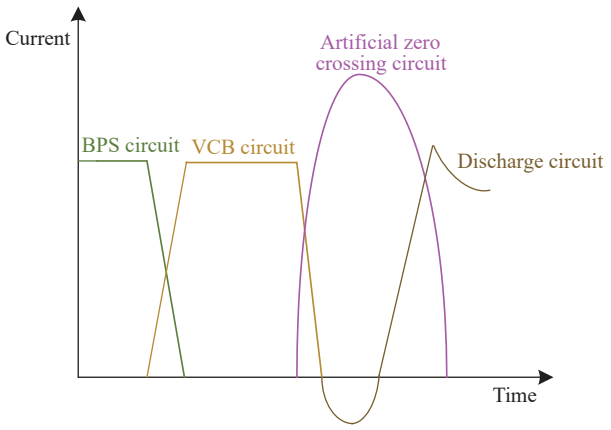

Fig. 2　Control logic and current transfer waveform of QPS

However, under high current conditions, the pulse inductor generates a magnetic field, which subjects the connecting devices within the auxiliary oscillation circuit of QPS to electromagnetic forces, leading to deformation. Consequently, the reliability of the QPS is significantly reduced. Therefore, it is necessary to analyze and optimize the magnetic field of pulse inductor.

In this paper, the working process and importance of pulsed inductors in the auxiliary oscillation zero-crossing circuit are introduced in detail. The magnetic induction intensity of the pulse inductor at any point in space can be calculated by using an equivalent mathematical model based on the physical model, and simulations can be used to determine the distribution of the magnetic field around the pulse inductor and how it affects the nearby equipment. The ideal selection of shielding plate material and shape is covered in this paper along with an electromagnetic shielding method that is suggested. The findings have broad repercussions for upcoming reliability research on auxiliary oscillation zero-crossing systems[16-18].

1　Theoretical calculation of pulse inductor

1.1　Design of electrical parameters of pulse inductor

In the QPS, the commutation circuit generates a high amplitude pulse current by using the charging capacitor to oscillate with a pulse inductor. The pulse current flows in reverse through the main circuit vacuum switch, creating an artificial zero-crossing point for it to shut down. A simplified diagram of the current transfer process is shown in Fig. 3.

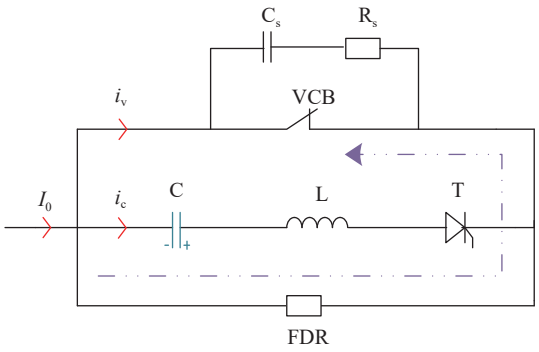

Fig. 3　Simplified diagram of current transfer process

In Fig. 3, the thyristor T control is turned on, and the charging capacitor and pulse inductor release the reverse pulse current to the vacuum switching branch, thus forcing the current down to achieve zero-crossing shutdown. Assuming that the thyristor is turned on at t_0, the VCB current decreases to zero at t_1. The analytical equations of the circuit in this process are obtained as follows:

$$I_0 = i_V + i_C \tag{1}$$

$$u_c = U_{co} - \frac{1}{C}\int i_C \mathrm{d}t \tag{2}$$

$$i_C = C\frac{\mathrm{d}u_c}{\mathrm{d}t} \tag{3}$$

In the above equation:

I_0 —— magnet current (A);

i_V —— VCB current (A);

i_C —— artificial zero-crossing loop current (A);

U_{co} —— charging capacitor voltage (V);

u_c —— capacitor voltage (V).

After derivation, the following equations are obtained.

$$i_V = I_0 - U_{co}\sqrt{\frac{C}{L}}\sin\left[\sqrt{\frac{1}{LC}}(t-t_0)\right] \tag{4}$$

$$i_V = I_0 - U_{co}\sqrt{\frac{C}{L}}\sin\left[\sqrt{\frac{1}{LC}}(t-t_0)\right] \quad (5)$$

$$u_c = U_{co}\cos\left[\sqrt{\frac{1}{LC}}(t-t_0)\right] \quad (6)$$

The pulse inductor in the converter communication circuit plays the role of regulating the pulse current width and controlling the pulse current amplitude and rate of change, and plays a vital role in whether the vacuum switch can be turned off reliably. Therefore, communication circuit parameters need to be calculated.

As shown in Fig. 4, the auxiliary oscillation zero-crossing circuit consists of charging capacitor C, pulse inductor L and thyristor bridges (T1, T2, T3, T4), which can realize bidirectional fault current opening and closing, S_1 is the charging circuit control switch of charging capacitor, R_c is the charging current limiting resistor; S_2 is the discharging circuit control switch, R_1 is the discharging resistor of charging capacitor.

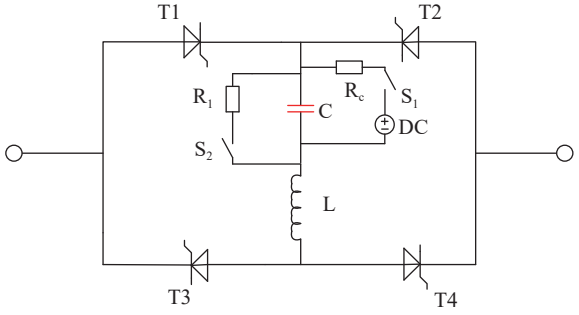

Fig. 4 Topology of auxiliary oscillation zero-crossing circuit for QPS

Based on the technical parameters in Tab. 1, the oscillation discharge loop parameters were determined. For the magnet supply voltage level, the preset voltage of the commutation circuit U_{co} is 12 kV, and the initial rise rate of the commutation pulse current is controlled below 190 A/μs, ignoring the influence of the thyristor bridge arm parameters on the commutation process.

Tab. 1 Technical parameters of commutation circuit

Technical parameters	Value
$\lvert di/dt\rvert_{max}$/(A·μs^{-1})	100~200
$\lvert du/dt\rvert_{max}$/(V·μs^{-1})	200~500
t_{com}/μs	⩾ 300
U_{co}/kV	5~12

$$\frac{U_c}{L} \leqslant 190\ \mathrm{A}/\mu\mathrm{s} \quad (7)$$

The calculation shows that $L \geqslant 63.2$ μH, the actual use of 66 μH.

Considering the current margin, taking the safety circulating current factor $k = 1.2$, the peak commutation I_P current is shown as Eq. (8):

$$I_P = U_c\sqrt{\frac{C}{L}} = kI_m = 1.2\times 100\ \mathrm{kA} = 120\ \mathrm{kA} \quad (8)$$

2 Inductor design and commutation problems

2.1 Pulse inductor design

Copper conductor[19] is chosen as the inductor material based on the pulse inductor's operating circumstances, the needed stray parameters, cost performance requirements, and space requirements. The circular design of the inductor coils, as seen in Fig. 5, effectively avoids the challenges presented by square solenoids and lessens the skin effect. The inductor's coils are roughly concentrically arranged, which can equally distribute magnetic stress on the coils and lessen electromagnetic force damage to the coil structure.

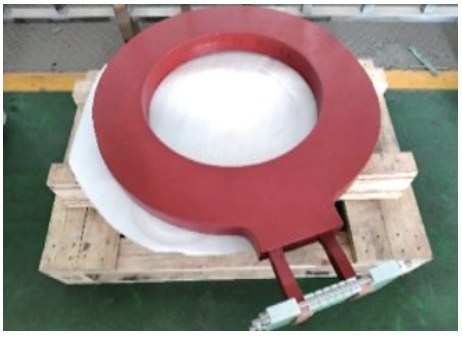

Fig. 5 Model diagram of pulse inductor

According to the model and relevant calculation parameters in Fig. 6 and Tab. 2, the simulation of the pulsed inductor operating at 120 kA operating condition is carried out in ANSYS, and the internal magnetic force line vector diagram and magnetic field cloud diagram of the coil are obtained. The simulation results are shown in Fig. 7 and Fig. 8.

As can be seen from Fig. 7 and Fig. 8, the pulse

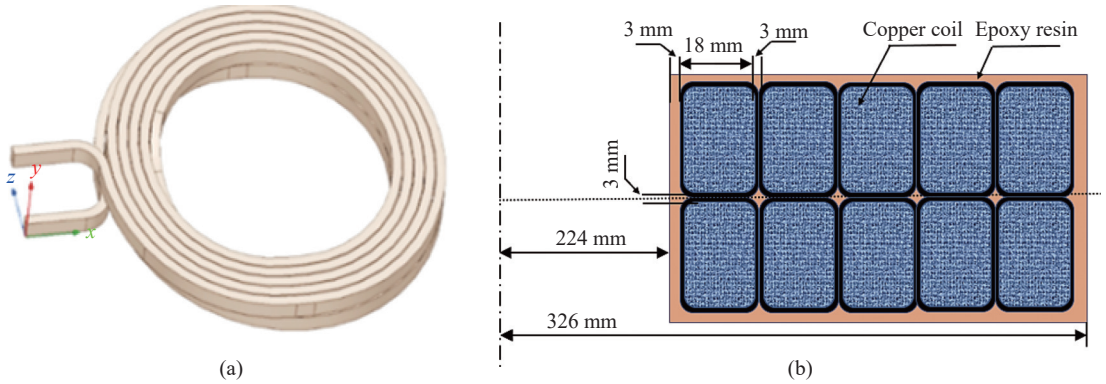

Fig. 6　3D model of pulse inductor coil

Tab. 2　3D finite element simulation to calculate the relevant parameters

Parameters	Values
Conductor dimension/mm×mm	25×18
Inside diameter/mm	448
Outside diameter/mm	652
Height/mm	53
Turn number/turn	5
Layer number/turn	2
Excitation current/kA	120
Current frequency/Hz	400

inductor's maximum magnetic induction intensity is 12.7 T for a 120 kA pulse current.

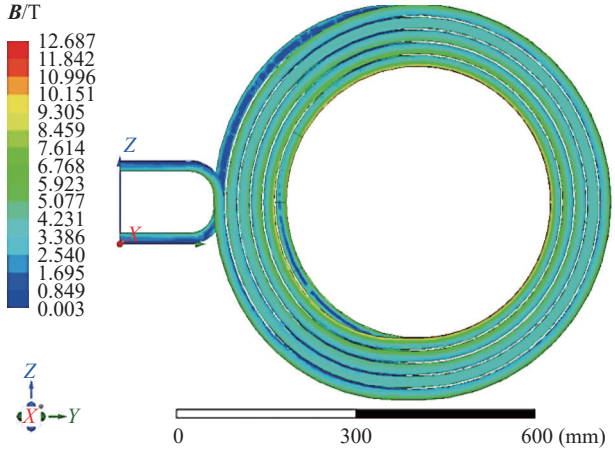

Fig. 7　Inner cloud diagram of coil

2.2　Analysis of oscillation discharge circuit problems

According to Fig. 9, when a pulse current of 120 kA is supplied during the experiment, the copper bar linked below the inductor would deform under the effect of the electromagnetic force, harming the equipment and

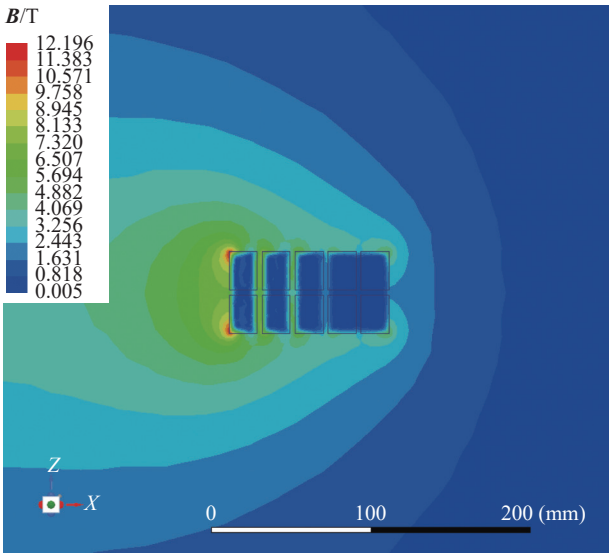

Fig. 8　Cloud image of surrounding magnetic field

significantly lowering the auxiliary oscillation zero-crossing circuit's reliability. Therefore, we consider adding a magnetic shielding plate underneath the inductor to reduce the impact of the magnetic field generated by the inductor on the connected copper bar, thus reducing the damage to the equipment.

In the paper, the concept of magnetic field shielding percentage S is introduced to measure the shielding effect to compare the shielding effect of the magnetic field. The defining equation is shown as Eq. (9):

$$S = \frac{\boldsymbol{B}_1 - \boldsymbol{B}_2}{\boldsymbol{B}_1} \times 100\% \qquad (9)$$

$\boldsymbol{B}_1$——the magnetic induction intensity when there is no shielding;

$\boldsymbol{B}_2$——the magnetic induction intensity with shielding.

(a) (b)

Fig. 9 Field diagram of connecting bar deformation

The model diagram of the connecting bar under the pulse inductor, shown in Fig. 10, is established according to the field object. The connecting bar is located under the pulse inductor and consists of six rectangular copper bars connected. To obtain the magnetic induction intensity on each connecting bar, it is numbered as shown in Fig. 11.

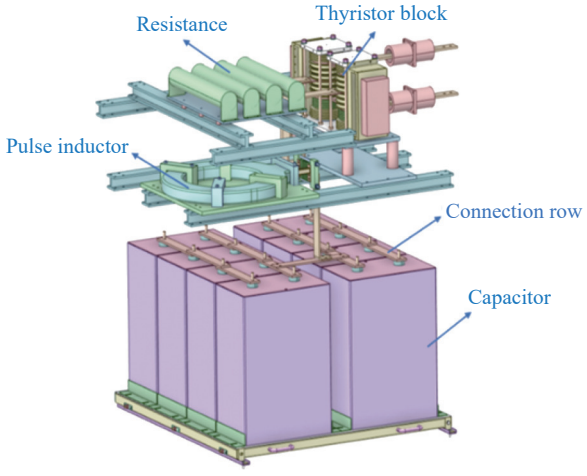

Fig. 10 Model diagram of auxiliary oscillation zero-crossing circuit

When 120 kA current passes through the pulse inductor, the change in magnetic field intensity of the connecting bar below is observed. Seven lines are taken evenly on each of the two plates, respectively, and 1 001 points are taken on each line. The lines are spaced 10 mm apart and oriented from side A to side C (plate 1)

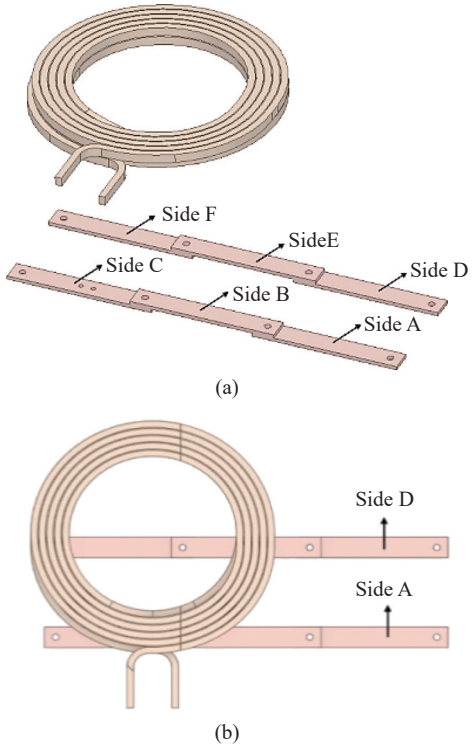

Fig. 11 Connecting bar model diagram

and from side D to side F (plate 2). The finite element simulation software Maxwell is used to simulate along the linear direction to get the magnetic induction intensity at different distances along the direction. The connecting bar point diagram is shown in Fig. 12.

According to Maxwell simulation, the magnetic

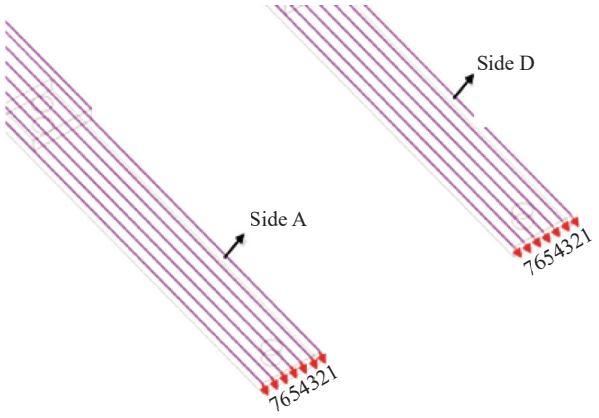

Fig. 12　Connecting bar point diagram

induction intensity of different points on different straight lines on the connecting bar is obtained, and the data is imported into Origin software to observe the magnitude of magnetic induction intensity at the edge and non-edge of the connecting bar, as well as the magnetic field distribution pattern.

The edge magnetic induction intensity magnitude tends to rise and then fall overall on plate 1 and plate 2 in Fig. 13. In the interval of 0.7 m to 0.9 m, the edge magnetic field intensity on the connecting bar is greater than other points and will be subject to greater electromagnetic force. In Fig. 14, The magnetic induction intensity of the connecting bar is the weakest and the electromagnetic force is the weakest in the non-edge area, between 0.4 m and 0.7 m of the plate. Therefore, it is necessary to shield the connecting bar to reduce the magnetic induction intensity of the connecting bar, reduce the deformation effect caused by the electromagnetic force, and improve the reliability of the system.

3　Electromagnetic shielding simulation analysis

3.1　Analysis of the influence of shielding metal plate material on shielding

First of all, eddy current shielding mainly uses high-conductivity shielding materials to generate eddy

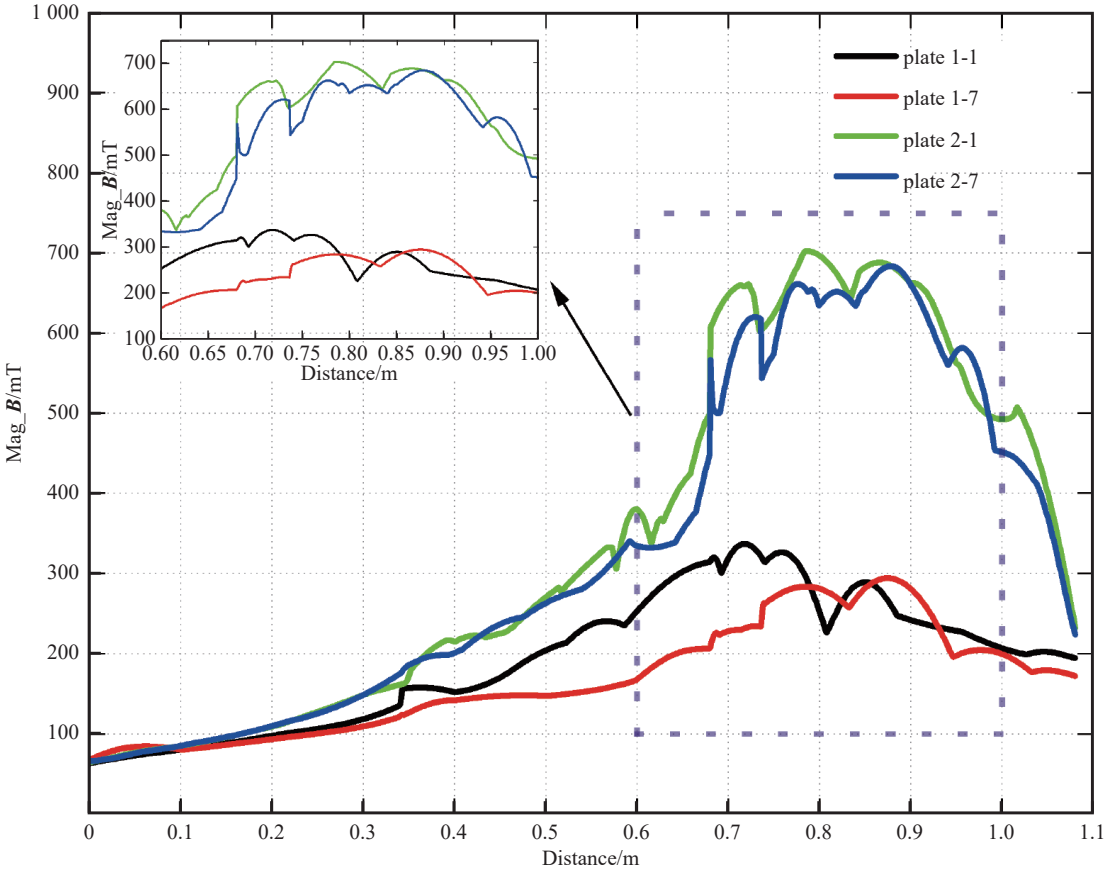

Fig. 13　Intensity change of magnetic field at the edge of connecting bar

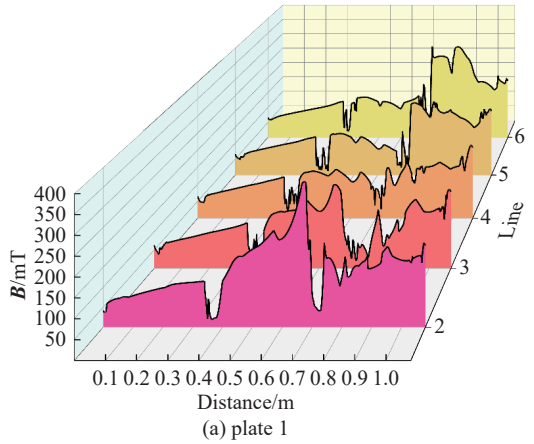

(a) plate 1

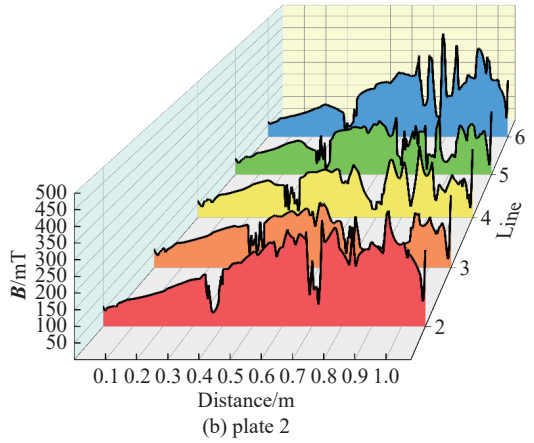

(b) plate 2

Fig. 14 Intensity change of magnetic field at the non-edge of connecting bar

currents under time-varying magnetic fields, thus generating a magnetic field opposite to the initial one and offsetting part of the original magnetic field. At the same time, the generated eddy currents will generate losses within the metal shielding body, strengthening the weakening of magnetic field energy, to achieve the shielding effect. Common materials include copper, tin, etc. The flux shunt principle is the use of high magnetic permeability materials, such as iron, nickel steel, and permalloy. The magnetic lines of force are bound within the magnetic material. It will change direction to achieve the shielding effect[20-21].

The more common shielding materials in engineering are aluminum, copper, and iron. In this section, aluminum, copper and iron are selected for analysis. The rectangular shield plate shielding is used for simulation. The relative permeability of aluminum and copper is 1, and the relative permeability of iron is taken as 500. The electrical conductivity of aluminum is: 3.82×10^7 S/m, copper is: 5.80×10^7 S/m, and iron is: 2.0×10^7 S/m.

Fig. 15 shows the magnetic induction intensity bar chart and shielding percentage line chart of different shielding materials, and compares the difference of shielding effect of different materials. In the selection of different materials for shielding plates, iron has the worst shielding effect, while aluminum and copper have similar shielding effects. Under economic consideration, aluminum is more economical than copper as the magnetic field shielding material. Therefore, aluminum is the best choice for shielding plate material.

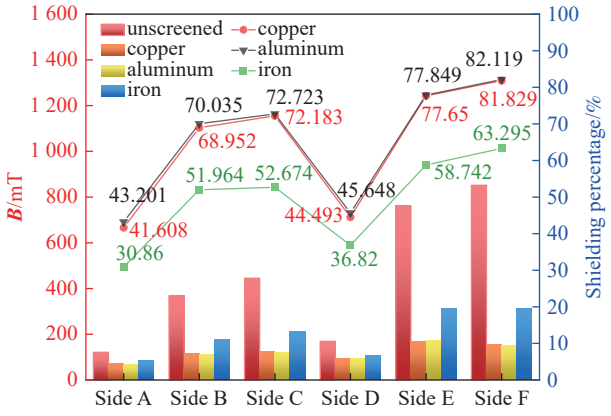

Fig. 15 Magnetic induction intensity and shielding percentage of different materials

3.2 Analysis of the influence of shield plate shape on shielding

For the alternating magnetic field in the shielded conductor caused by eddy currents, eddy currents in the shielding body produce skin effect. The skinning depth of aluminum at 400 Hz was calculated as 4.07 mm, so the thickness of the plate was taken as 5 mm.

Considering the magnetic field intensity distribution and material economy of the pulsed inductor, three shielding structures are proposed below, as shown in Fig. 16. Using Maxwell software, the magnitude of the magnetic induction intensity applied to the connecting bars under different structures is compared.

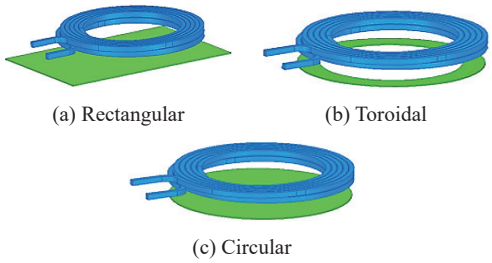

Fig. 16　Shield plate construction

Fig. 17 shows the magnetic induction intensity bar chart and shielding percentage line chart under different shielding structures, and compares the influence of different shapes on shielding effectiveness. The comparison shows that there are significant differences in the shielding effects from different shielding structures.

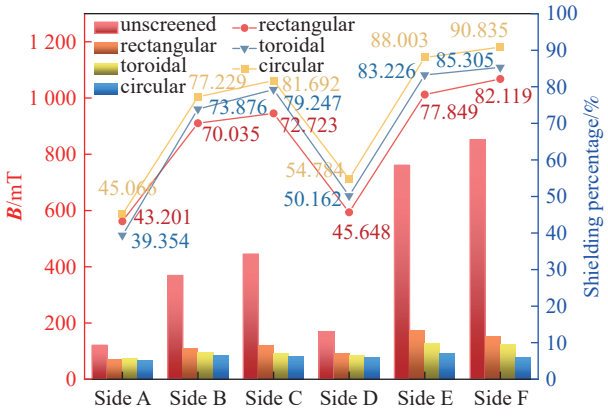

Fig. 17　Magnetic induction intensity and shielding percentage of different structures

In Fig. 17, for the circular shielding structure, the magnetic induction intensity of the connecting bar is the smallest. A circular shielding plate is a closed structure that can effectively reduce the penetration of radiation energy, and the surface eddy currents are more uniform and denser, making it easier to form a closed loop. In the toroidal shielding plate, due to the presence of intermittent structures, the eddy current effect may be disturbed or interrupted, leading to instability of the shielding effect or leakage of the magnetic field in some areas. The interference of magnetic leakage and eddy current paths at the edge of the rectangular shielding plate leads to local concentration of the electromagnetic field, thereby reducing the shielding effect. The final choice of a circular shielding plate can effectively reduce the magnetic induction intensity of the connecting bar and improve the reliability of the system.

3.3　Calculation of eddy current loss of shield plate

Eddy current loss will result from the alternating magnetic field's impact on the shield plate at high current conditions. It causes energy loss and lowers the effectiveness of the shield. Furthermore, it will cause the shielding equipment's temperature to rise. As a result, the design should aim to reduce eddy current loss as much as possible, and the right shielding structure should be chosen.

$$I_t = \int_\Omega J \mathrm{d}\Omega = \int_\omega \frac{1}{\mu}(\sigma + \mathrm{j}\omega\epsilon)(-\mathrm{j}\omega A - \nabla\varnothing)\mathrm{d}\omega \quad (10)$$

$$F = \frac{1}{2}\int R_e |J \times B| \mathrm{d}V \quad (11)$$

Ohmic-loss calculation formula is shown as Eq. (12).

$$P_{\text{ohmic-loss}} = \int_V \frac{JJ^*}{2\sigma}\mathrm{d}V \quad (12)$$

Where:

I_t —— total current (A);

μ —— permeability of medium (H/M);

σ —— conductivity (S/M);

$\nabla\varnothing$ —— gradient of potential (T/M);

F —— electromagnetic force (N);

R_e —— the real part of a complex number;

B —— magnetic field strength vector (T).

The ohmic loss of the shield plate under various structures is obtained by simulation using a 120 kA current flowing into a three-dimensional time-harmonic field, as shown in Tab. 3.

Tab. 3　Ohmic loss of different shielding structures

Shielding structure	Ohmic loss/(MW·m^{-3})
Rectangular	32.733
Toroidal	31.761
Circular	11.199

Because the model contains multiple conductors, the surface integral of the ohmic-loss density on different shielding bodies is calculated using a field computer, and the eddy current losses of various

shielding structures are calculated.

Comparatively, as shown in Tab. 4, the eddy current loss of the toroidal shield plate is the greatest, while that of the rectangular and circular shield plates is comparable. The circular shield is better when taking shape and material into consideration.

Tab. 4 Eddy current loss of different shielding structures

Shielding structure	Eddy current loss/MW
Rectangular	21.668
Toroidal	29.185
Circular	21.957

3.4 Structure simulation

According to Maxwell, it was possible to determine the magnetic induction intensity of the connecting bars under various shielding structures. By mapping the results synchronously in the mechanical field, it is possible to see how different shielding structures affect the deformation of the connecting bar.

In a three-dimensional Mechanical, the two ends of the connecting bar are fixed. Considering practical factors, the connecting bar is affected not only by the electromagnetic force transmitted by Maxwell but also by its gravity. In Fig. 18, it is found that the deformation of the connecting bar mainly occurs in the middle part, which is also the place where the electromagnetic force is the greatest.

The calculation results are shown in Tab. 5. Calculate the electromagnetic force and equivalent stress on the connecting bar of different shielding structures. The equivalent stress is much lower than the 250 MPa yield strength of the connecting bar, and the safety margin is sufficient. When the pulse inductor is not shielded, the maximum deformation of the connecting bar reaches 1.974 mm. The connecting bar

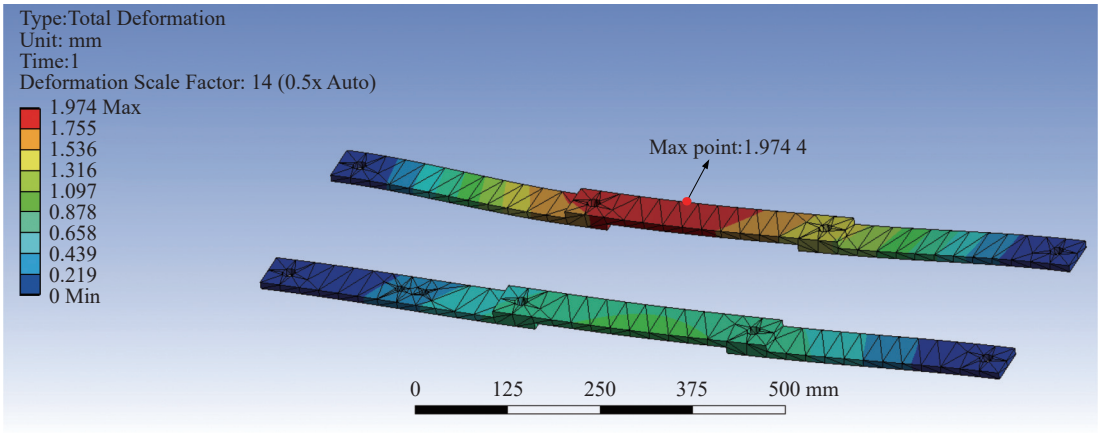

(a) Unshielded structure

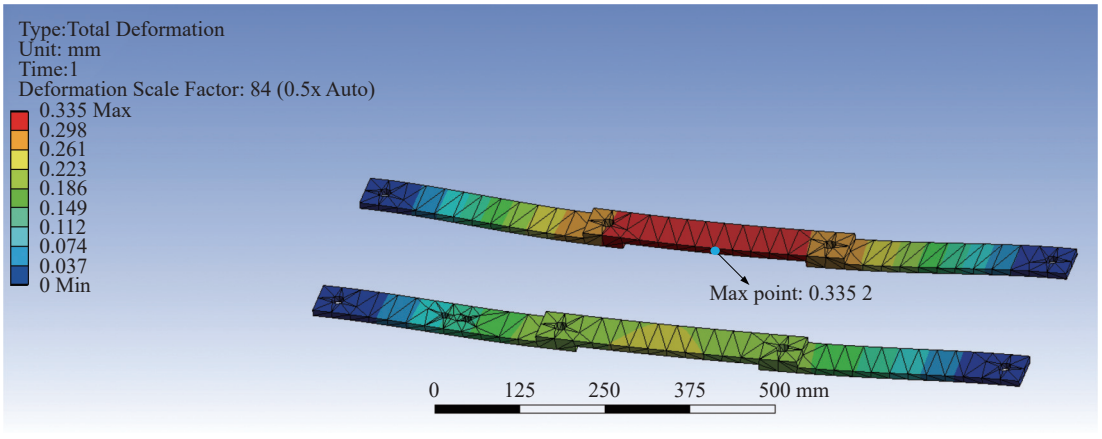

(b) Rectangular shielding structure

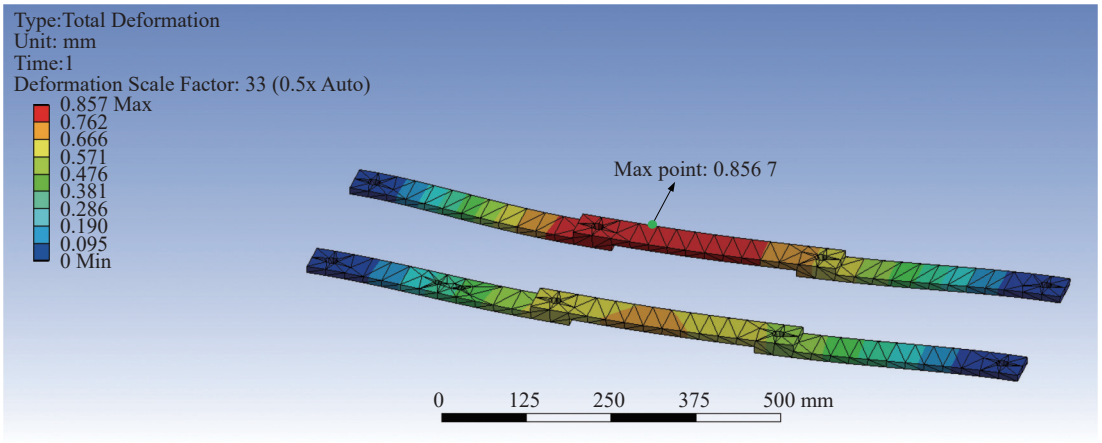

(c) Toroidal shielding structure

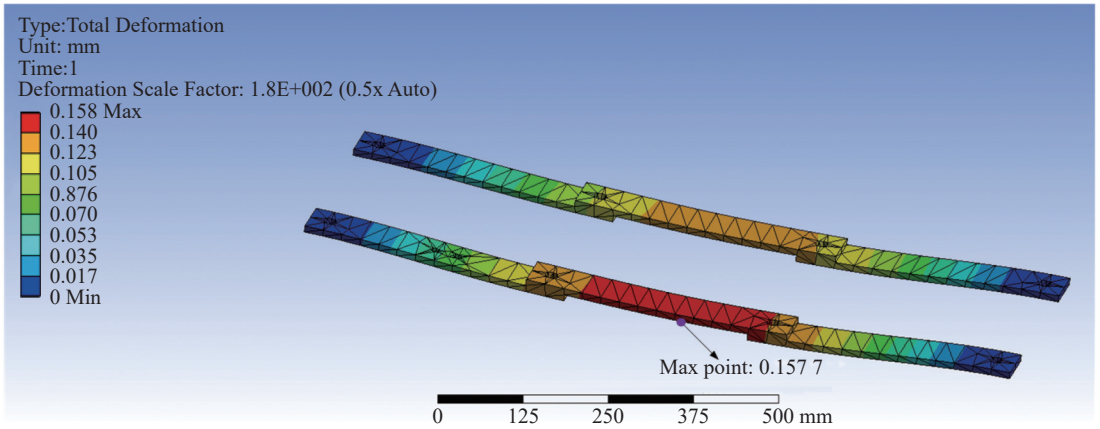

(d) Circular shielding structure

Fig. 18　Deformation of connecting bar under different shielding structures

variable is significantly lessened by masking. Among them, the circular shield structure has the best effect, with the maximum shape variable of 0.158 mm and the average shape variable of 0.079 mm. This successfully lessens the impact of the electromagnetic force produced by the pulsed inductor on the surrounding machinery.

Tab. 5　Connecting bar deformations under different shielding structures

Shielding structure	Connecting bar electromagnetic force/N	Equivalent stress/ MPa	Maximum deformation/ mm	Average deformation/ mm
Unshielded	809.630	—	1.974	0.712
Rectangular	264.320	13.6	0.335	0.157
Toroidal	467.810	30.5	0.857	0.420
Circular	72.185	10.3	0.158	0.079

#Note: The yield strength of copper is 250 MPa, and the ultimate tensile strength is 343 MPa.

4　Conclusion

In this article, when the shielding plate material is aluminum, the pulse inductor has the best optimization effect on the electromagnetic field distribution of the connecting bar. When considering the shielding plate structure, the shielding effect of circular shielding plates is the most ideal. In summary, the use of circular aluminum shielding plates can effectively reduce the magnetic induction intensity and electromagnetic force of the connecting bar, and improve the overall reliability of the QPS. However, the simulation in this article only analyzes and calculates the influence of shielding plate materials and structures on the electromagnetic distribution of pulse inductors. Therefore, this conclusion will be verified through experiments in the

next step, and other factors affecting the shielding effect will be considered.

参考文献：

[1] FURTH H P. Magnetic confinement fusion［J］. Science, 1990, 249(4976): 1522-1527. DOI: 10.1126/science.249.4976.1522.

[2] WAN B N, DING S Y, QIAN J P, et al. Physics design of CFETR: determination of the device engineering parameters［J］. IEEE transactions on plasma science, 2014, 42(3): 495-502. DOI: 10.1109/TPS.2013.2296939.

[3] 许强林, 李华, 宋执权, 等. CFETR 失超保护系统总体设计研究［J］. 南方能源建设, 2022, 9(2): 33-38. DOI: 10.16516/j.gedi.issn2095-8676.2022.02.004.
XU Q L, LI H, SONG Z Q, et al. Research on overall design of quench protection system for CFETR［J］. Southern energy construction, 2022, 9(2): 33-38. DOI: 10.16516/j.gedi.issn2095-8676.2022.02.004.

[4] GAVRILIN A V, EYSSA Y M. Modeling of electromagnetic and thermal diffusion in a large pure aluminum stabilized superconductor under quench［J］. IEEE transactions on applied superconductivity, 2001, 11(1): 2599-2602. DOI: 10.1109/77.920400.

[5] MARTOVETSKY N, MICHAEL P, MINERVINI J, et al. Test of the ITER central solenoid model coil and CS insert［J］. IEEE transactions on applied superconductivity, 2002, 12(1): 600-605. DOI: 10.1109/TASC.2002.1018475.

[6] WENG P D, BI Y F, CHEN Z M, et al. HT-7U TF and PF conductor design［J］. Cryogenics, 2000, 40(8/10): 531-538. DOI: 10.1016/S0011-2275(01)00009-1.

[7] FANG J, CHEN Z M, WU S T, et al. Research of the CICC stability by the numerical code Gandalf［J］. Plasma science and technology, 2000, 2(4): 383-396. DOI: 10.1088/1009-0630/2/4/008.

[8] 方进, 翁佩德, 陈灼民, 等. 运行温度对 NbTi 管内电缆导体瞬态稳定性的影响实验研究与分析［J］. 中国电机工程学报, 2003, 23(4): 113-118. DOI: 10.13334/j.0258-8013.pcsee.2003.04.023.
FANG J, WENG P D, CHEN Z M, et al. Experimental research and analysis of the influence of operating temperature on NbTi CICC transient stability［J］. Proceedings of the CSEE, 2003, 23(4): 113-118. DOI: 10.13334/j.0258-8013.pcsee.2003.04.023.

[9] TANG C W, LI H, SONG Z Q, et al. Design and characterisation of the high-current DC breaker driven by explosive［J］. High voltage, 2023, 8(3): 466-476. DOI: 10.1049/hve2.12286.

[10] GAIO E, NOVELLO L, PIOVAN R, et al. Conceptual design of the quench protection circuits for the JT-60SA superconducting magnets［J］. Fusion engineering and design, 2009, 84(2/6): 804-809. DOI: 10.1016/J.FUSENGDES.2008.12.100.

[11] FU P, SONG Z Q, GAO G, et al. Quench protection of the poloidal field superconducting coil system for the EAST tokamak［J］. Nuclear fusion, 2006, 46(3): S85-S89. DOI: 10.1088/0029-5515/46/3/S11.

[12] 江加福, 刘小宁, 许留伟, 等. 基于 EAST 超导纵场线圈的换流分析［J］. 高电压技术, 2009, 35(1): 186-191. DOI: 10.13336/j.1003-6520.hve.2009.01.010.
JIANG J F, LIU X N, XU L W, et al. Analysis of discharge based on toroidal field coils of EAST［J］. High voltage engineering, 2009, 35(1): 186-191. DOI: 10.13336/j.1003-6520.hve.2009.01.010.

[13] SONG I, ROSHAL A, TANCHUK V, et al. The fast discharge system of ITER superconducting magnets［C］//2011 International Conference on Electrical Machines and Systems, Beijing, August 20-23, 2011. Beijing: IEEE, 2011: 1-6. DOI: 10.1109/icems.2011.6073779.

[14] 杜华珠, 文习山, 鲁海亮, 等. 35 kV 三相空心电抗器组的磁场分布［J］. 高电压技术, 2012, 38(11): 2858-2862. DOI: 10.3969/j.issn.1003-6520.2012.11.011.
DU H Z, WEN X S, LU H L, et al. Magnetic field distribution around 35 kV three-phase air-core reactors［J］. High voltage engineering, 2012, 38(11): 2858-2862. DOI: 10.3969/j.issn.1003-6520.2012.11.011.

[15] 孙爱良. 环形电流平面内的磁场［J］. 兰州铁道学院学报, 1999, 18(1): 98-101.
SUN A L. The magnetic field in the plane of circle electric current［J］. Journal of Lanzhou railway institute, 1999, 18(1): 98-101.

[16] 李华, 宋执权, 汪舒生, 等. 核聚变装置中直流保护开关的研究进展［J］. 中国电机工程学报, 2016, 36(增刊 1): 233-239. DOI: 10.13334/j.0258-8013.pcsee.161406.
LI H, SONG Z Q, WANG S S, et al. Study on DC protection switch for superconducting coils in magnetic confinement fusion device［J］. Proceedings of the CSEE, 2016, 36(Suppl.1): 233-239. DOI: 10.13334/j.0258-8013.pcsee.161406.

[17] 宋执权, 傅鹏, 汤伦军, 等. EAST 极向场电源失超保护系统的设计及模拟实验［J］. 核聚变与等离子体物理, 2007, 27(1): 28-33. DOI: 10.3969/j.issn.0254-6086.2007.01.006.
SONG Z Q, FU P, TANG L J, et al. Design of the quench protection system of the EAST PFPS and its simulation［J］. Nuclear fusion and plasma physics, 2007, 27(1): 28-33. DOI: 10.3969/j.issn.0254-6086.2007.01.006.

[18] HU X G, LI H, SONG Z Q, et al. Concept design of 100 kA hybrid DC breaker on China fusion engineering test reactor［J］. Fusion engineering and design, 2020, 158: 111740. DOI: 10.1016/j.fusengdes.2020.111740.

[19] TONG W, LI C, SONG Z Q, et al. Preliminary design of pulse inductor applied for 100-kA quench protection system［J］. IEEE transactions on plasma science, 2020, 48(6): 1754-1761. DOI: 10.1109/TPS.2020.2971774.

[20] MEYER E S, SILVERA I F, BRANDT B L. Eddy current shielding and heating: reduction of dissipation for very low-

temperature experiments in the presence of magnetic field ripple [J]. Review of scientific instruments, 1989, 60(9): 2964-2968. DOI: 10.1063/1.1140636.

[21] 赵灵智, 胡社军, 何琴玉, 等. 电磁屏蔽材料的屏蔽原理与研究现状 [J]. 包装工程, 2006, 27(2): 1-4,15. DOI: 10.3969/j.issn.1001-3563.2006.02.001.

ZHAO L Z, HU S J, HE Q Y, et al. Shielding principle and research progress of electromagnetic shielding materials [J]. Packaging engineering, 2006, 27(2): 1-4,15. DOI: 10.3969/j.issn.1001-3563.2006.02.001.

作者简介：

李振瀚

李振瀚（第一作者）

1997-, Male, PhD student, school of electrical engineering and automation, Hefei University of Technology, mainly engaged in the research of electromagnetic field optimization and quench protection (e-mail) zhenhan.li@ipp.ac.cn.

李华

李华（通信作者）

1984-, Male, PhD, associate researcher of Institute of Plasma Physics, Chinese Academy of Sciences, mainly engaged in the research of electric machine drives, high-voltage high-frequency converters, and high-power DC breakers (e-mail) lihua@ipp.ac.cn.

鲍晓华

1972-, Male, professor of Hefei University of Technology, PhD, mainly engaged in the research of motor design theory and technology, motor electromagnetic field theoretical analysis and calculation, large motor and high and low speed Electric machine (e-mail) sukz@ustc.edu.

高格

1975-, Female, PhD, researcher of Institute of Plasma Physics, Chinese Academy of Sciences, mainly engaged in the research of tokamak magnet power supply and its control technology (e-mail) gg@ipp.ac.cn.

项目简介：

项目名称　聚变堆主机关键系统综合研究设施（2018-000052-73-01-001228）

承担单位　项目法人单位：中国科学院合肥物质科学研究院 等离子体物理研究所；参建单位：中国核工业集团公司核工业西南物理研究院。

项目概述　设施主要建设内容为超导磁体研究系统和偏滤器研究系统。超导磁体研究系统主要建设材料综合性能研究平台、导体性能研究平台、磁体性能研究平台、环向场磁体、中心螺管模型线圈磁体、高温超导磁体、低温系统及电源系统。偏滤器研究系统主要建设偏滤器等离子体与材料相互作用研究平台、偏滤器部件工程测试平台、偏滤器原型部件、全超导托卡马克核聚变实验装置下偏滤器、1/8 真空室及总体安装系统、负离子源中性束注入系统、电子共振加热系统、高场低杂波电流驱动系统、离子回旋加热系统、遥操作系统、总控系统等。

主要创新点　本设施科学目标是开展磁约束聚变堆边界参数下的等离子体行为研究，探究主机关键系统和部件复杂动态负荷对主机系统可靠性、稳定性、安全性的影响，评估偏滤器与超导磁体材料/部件在堆工情况下的服役性能，为我国开展聚变堆设计及核心部件研发、热与粒子排除关键问题研究、大规模低温和超导技术研究、强流离子束与基础等离子体研究、深空探索等提供技术支撑。工程目标是建成参数高、功能完备的综合性研究设施。

（编辑　徐嘉铖）